Beam Vibration Displacement Curve Measurement

Marcellin Zahui and Rohan Thomas

University of North Dakota, Grand Forks, ND 58201, USA

Beam dynamics are often measured using accelerometers and in some cases laser based systems. Natural frequencies, modes shapes, and deflections are then derived from these measurements. The work presented here describes a method to directly measure the deflection curve of a vibrating beam using piezoelectric films. The sensor consists of a constant shape PolyVinyliDene Fluoride (PVDF) film bonded to the surface of the beam and spanning the entire beam length. Bands parallel to the width of the beam are etched on the film to create multiple separate sections of the sensor on the lower electrode. The individual output charge of the sensor sections is shown to be proportional to the slope of the beam lateral displacement curve at the location of the patch or section. The beam surface lateral displacement curve is calculated from the slopes using the central difference method. The equation of the sensor is derived along with errors analysis followed by numerical and multiphysics simulation. The results show that the proposed sensor can be used to effectively measure the lateral vibration displacements of prismatic beams with various boundary conditions. Furthermore, acceleration measurements on a clamped-clamped beam are used to validate the sensor design. It is shown in the paper that the accuracy of the sensor is closely related to the number of sensor sections and the target highest frequency. Thus, a relatively large number of measurement channels may be needed depending on the required accuracy of the measurements and the highest frequency in the excitation.

1. INTRODUCTION

Actuators and sensors play a central role in active vibration control, acoustic emission monitoring, nondestructive testing, structure health monitoring, and many other types of applications.[1] In the last three decades or so, the design of the actuators and sensors has been focused on piezo films,[2] especially on the use of PVDF, which is a piezoelectric polymer that can be poled in thin films down to 9 micron.[3] This makes them suitable for sensor development because they add little loading to the receiving structure and are easy to cut, shape, and etch.[4]

Many applications of PVDF based sensors can be found in literature in active noise and vibration control,[5] material characterization,[6] the medical field,[7] etc. PVDF is usually in the form of a film that is bonded to the structure.[8] To cite but a few, recent applications of PVDF as actuator involved a vibrating membrane used for fatigue test of thin films.[9] Another application uses PVDF laminate as an actuator to control the vibration of a cylindrical shell.[10] In these applications, multiple layers of film are used to increase the available actuating force. However for sensing, the ideal situation is to use as minimum number of layers as possible so that the sensor does not interfere with the structure's dynamic properties. In general, the film is very flexible compared to the structure to which it is bonded. Therefore, the strain transferred to the structure is expected to be very small. The film is usually shaped[11] to extract the dynamic properties of interest. Researchers have measured the volume velocity of beams and plates for active noise and vibration cancellation[12] using quadratic functions to shape the sensor film while others have used a mixture of quadratic and linear functions to shape sensors that measure localized volume velocity.[13]

The current paper presents the framework for the measurement of the lateral displacements of a vibrating beam using distributed sensor for various boundary conditions. Generally, well established point sensors such as accelerometers are used to measure the dynamic properties of vibrating structures. However for control systems, especially since the advent and wide spread of active control and structural health monitoring, researchers have been looking for more non-conventional sensors (mainly distributed sensors). In the case of active vibration control, distributed sensors tend to provide better vibration properties of the controlled structure. Unlike point sensors, distributed sensors can give simultaneous measurement data for various locations on the structure and are less likely to miss a vibration mode. For example, a point sensor on a relatively long beam could provide a false reading of the state of the beam if its location corresponds to a vibration node.[14]

One particular promising application that motivated the investigation of the proposed sensor is the monitoring of the structural supports of signs, luminaires, and traffic signals.[15] Various vibration mitigation devices have been proposed for these structural supports with no clear solution on how to assess their effectiveness. The sensor presented here could be an affordable solution for evaluating and monitoring the effectiveness of the vibration-mitigation[16] devices of structural supports of signs, luminaires, and traffic signals.

The proposed sensor can also be used in active vibration and noise control or structural members health monitoring. The sensor measures the slopes of the beam simultaneously at multiple locations on the beam to yield the instantaneous real time vibration curves. Important beam mechanical entities such as strains and stresses can be readily computed from the deflection curves making the proposed sensor an invaluable asset in control and structural health monitoring. Dynamic properties such as natural frequencies and mode shapes can also be calculated from the instantaneous deflection curves.

Strain based dynamic point sensors have been around for decades. These sensors use internal beams[17] to relate the dynamic properties of the structure to the strain on the surface of the beam. The strain at any point on the cantilever beam is proportional to the deflection of the mass. Therefore, the displacement of the base and the motion of the corresponding point on the structure can be found. The sensor proposed here extends

to the cantilever beam sensor concept with the strain sensor (PVDF) directly attached to the structure. Multiple sections of the sensor is used to measure the strain at multiple locations on the beam and translate those strains into displacements along the beam length. It is therefore obvious that the accuracy of the measurement will depend on the numbers of sensor sections relative to the highest target frequency.[18] The proposed displacement sensor approach presented here is made possible by the availability and cost of PVDF films, etching processes, and single chip computers.

2. SENSOR DESIGN

2.1. Generic Piezoelectric Film Output Charge Equations

A piezoelectric film bonded to a flexible shell continuum is totally covering the surface of the structure. The film is much thinner than the shell structure such that the strains in the film are assumed constant and equal to the outer surface strains of the shell. Also, the piezoelectric film is perfectly coupled with the shell continuum but does not change its dynamic characteristics i.e., natural frequencies and mode shapes. For such a thin film, only the transverse electric field E_3 is considered. Using direct piezoelectric equations for linear piezoelectricity[19] and Fig. 1 the voltage across the electrodes can be written as shown in Eq. (1):

$$\phi_3 = - \int\limits^{h_f} E_3 d\alpha_3; \qquad (1)$$

where h_f is the piezoelectric film layer thickness. From Fig. 1, the above equation can be expressed in term of normal strains in the film S_{11}^f and S_{22}^f in the direction of α_1 and α_2 respectively, and the electric displacement vector D_3.

$$\phi_3 = h^f \left(h_{31} S_{11}^f + h_{32} S_{22}^f - \beta_{33} D_3 \right); \qquad (2)$$

where β_{33} and h_{ij} denote respectively the impermeability and the strain charge coefficients of the piezoelectric film. The above voltage can be integrated over the entire film surface and yield the following equation:

$$
\begin{aligned}
\phi\left(\alpha_1, \alpha_2\right) = & \\
\frac{h^f}{S^f} \int\limits_{S^f} & \left[\left[h_{31} \left\{ \left[\frac{1}{A_1} \frac{\partial u_1}{\partial \alpha_1} + \frac{u_2}{A_1 A_2} \frac{\partial A_1}{\partial \alpha_2} + \frac{u_3}{R_1} \right] \right. \right. \right. \\
& + r_1^f \left[\frac{1}{A_1} \frac{\partial}{\partial \alpha_1} \left(\frac{u_1}{R_1} - \frac{1}{A_1} \frac{\partial u_3}{\partial \alpha_1} \right) \right. \\
& \left. \left. + \frac{1}{A_1 A_2} \frac{\partial A_1}{\partial \alpha_2} \left(\frac{u_2}{R_2} - \frac{1}{A_2} \frac{\partial u_3}{\partial \alpha_2} \right) \right] \right\} \\
& + h_{32} \left\{ \left[\frac{1}{A_2} \frac{\partial u_2}{\partial \alpha_2} + \frac{u_1}{A_1 A_2} \frac{\partial A_2}{\partial \alpha_1} + \frac{u_3}{R_2} \right] \right. \\
& + r_2^f \left[\frac{1}{A_2} \frac{\partial}{\partial \alpha_2} \left(\frac{u_2}{R_2} - \frac{1}{A_2} \frac{\partial u_3}{\partial \alpha_2} \right) \right. \\
& \left. \left. \left. \left. + \frac{1}{A_1 A_2} \frac{\partial A_2}{\partial \alpha_1} \left(\frac{u_1}{R_1} - \frac{1}{A_1} \frac{\partial u_3}{\partial \alpha_1} \right) \right] \right\} \right] \right] dS^f; \quad (3)
\end{aligned}
$$

where u_1, u_2, and u_3 are the shell displacements in the three principal direction of α_1, α_2, and α_3 respectively. r_1^f and r_2^f denote respectively the distances from the neutral surface to the bottom and top plane of the piezoelectric film layer. S
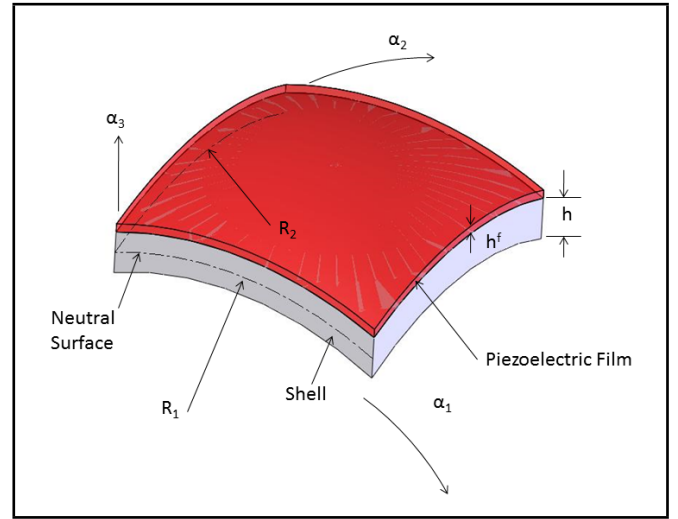

Figure 1. Shell covered with PVDF film.

is the shell or film area. Finally, A_1 and A_2 are the Lamé parameters[20] from the fundamental equation:

$$(ds)^2 = A_1^2 (d\alpha_1)^2 + A_2^2 (d\alpha_2)^2. \qquad (4)$$

Considering Eq. (3), Zou showed that the output of the piezoelectric film can be calculated analytically for simple structures such as beam and plates if u_1, u_2, and u_3 are known. However, for complex structures and boundary conditions, analytical solution is impossible.

2.2. Plate Substrate

Equation (3) can be further simplified if the film is bonded to a plate structure undergoing transverse motion and thus $R_1 = R_2 = \infty$. The Lamé parameters are derived from the fundamental equation $(ds)^2 = (1)^2 (dx)^2 + (1)^2 (dy)^2$ and therefore $A_1 = A_2 = 1$. Substituting these values into Eq. (3) and setting $z = u_3$ gives the piezoelectric film output charge as:

$$\phi = -\frac{h^f}{S^f} \int\limits_{S^f} \left[h_{31} r_x^f \frac{\partial^2 z}{\partial x^2} + h_{32} r_y^f \frac{\partial^2 z}{\partial y^2} \right] dS^f. \qquad (5)$$

2.3. Beam Substrate

If only one axis is considered, then the beam equation can be obtained from Eq. (5) as shown below by removing h_{32} term and setting $dS^f = b dx$ where b is the width of the beam.

$$\phi = -\frac{b h^f}{S^f} \int\limits_{x} \left(h_{31} r_x^f \frac{\partial^2 z}{\partial x^2} \right) dx. \qquad (6)$$

2.4. Sensor Equation

In the following, the beam substrate and Eq. (6) is considered. If multiple patches of film are used as shown in Fig. 2 with n segments of films, the ith patch output charge can be written from Eq. (6) in the form of.[21]

$$\phi_i = -\frac{b h_i^f}{S_i^f} \int\limits_{x_{i-1}}^{x_i} \left(h_{31_i} r_{x_i}^f \frac{\partial^2 z_i}{\partial x^2} \right) dx. \qquad (7)$$
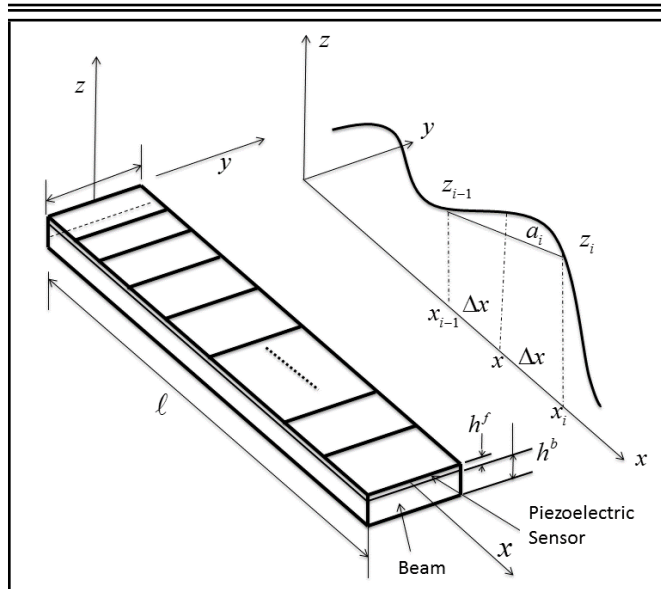
Figure 2. Beam covered with PVDF film and Beam deflection curve.

After integration, Eq. (7) yields the following equation:

$$\phi_i = -\frac{bh_i^f}{S_i^f}h_{31_i}r_{x_i}^f\left[\frac{\partial z_i}{\partial x}\right]_{x_{i-1}}^{x_i}. \qquad (8)$$

If the slope of the beam deflection is assumed constant at the location of the ith patch and set equal to a_i, then Eq. (8) can be written as:

$$\phi_i = -\frac{bh_i^f}{S_i^f}h_{31_i}r_{x_i}^f a_i. \qquad (9)$$

It can be seen from Eq. (9) that the ith film patch output signal is proportional to the slope of the displaced patch. Then the slope a_i can be written in term of the charge ϕ_i.

$$a_i = -\frac{\phi_i S_i^f}{bh_i^f h_{31_i}r_{x_i}^f}. \qquad (10)$$

Equation (9) represents the sensor general equation from which the slope of the beam section at the location of the sensor patch can be calculated using Eq. (10).

2.5. Beam Lateral Displacement Equation

The function z in Fig. 2 represents the deflection of the beam that can be evaluated at points that lie to the left and right of the center point x of the ith patch. Thus, the central-difference formula for the slop of z at the center of the patch is

$$a_i \cong \frac{z(x + \Delta x) - z(x - \Delta x)}{2\Delta x}. \qquad (11)$$

Setting $z_{i-1} = z(x - \Delta x) = z(x_{i-1})$, $z_i = z(x + \Delta x) = z(x_i)$, and $2\Delta x = x_i - x_{i-1}$, Eq. (11) becomes:

$$z_i \cong a_i(x_i - x_{i-1}) + z_{i-1}. \qquad (12)$$

The combination of Eq. (10) and Eq. (12) can be further simplified. For practical purposes, let's assume that the piezoelectric patches are of equal sizes and fabricated from the same uniform thickness film such that:

$$x_i - x_{i-1} = \frac{\ell}{n}, \quad r_{x_i}^f = \frac{h^f + h^b}{2} \cong \frac{h_b}{2}, \quad h_{31_i} = h_{31}. \quad (13)$$

Table 1. Error analysis results for a simply supported bean .

δx	z_m (Eq. (17))	z (Exact)	$\%E(z_m - z)$	$\%E$(Eq. (18))
$\ell/4$	0.508320369	0.587785252	13.52	11.38
$\ell/10$	0.298783216	0.309016994	3.31	3.18
$\ell/15$	0.204862754	0.207911690	1.47	1.44
$\ell/20$	0.155145721	0.156434465	0.82	0.82

Equation (12) becomes:

$$z_i = -2\frac{\phi_i \ell^2}{h^f h_b h_{31}n^2} + z_{i-1}. \qquad (14)$$

Equation (14) represents the general form of the beam lateral displacement equation and is independent of the beam boundary conditions. However, z_0 must be known to apply these equations. Therefore, the requirement on this method is that the displacement of at least one end of the beam must be known. For clamped and simply supported boundary conditions, the vector $\{z\}$ of z_i represents an approximation of the curve shown in Fig. 2. For any other boundary conditions, a point sensor near the origin can be used to find z_0.

2.6. Error Analysis

The beam deflection calculated from the sensor output is based on the central difference equation Eq. (11). This equation is approximating the slope of the beam deflection curve at the center of th ei^{th} patch. The exact slope can be written as:[22]

$$a_i = \frac{z(x + \Delta x) - z(x - \Delta x)}{2\Delta x} + E_t(z, \Delta x); \qquad (15)$$

where $E_t(z, \Delta x)$ is the truncation error so using a point x_c on the curve between x_{i-1} and x_i , the truncation error can be written as:

$$E_t(z, \Delta x) = \frac{(\Delta x)^2 z'''(x_c)}{6}. \qquad (16)$$

For a known slope z_i, the error on the deflection at $x + \Delta x$ can be derived as follows:

$$z(x + \Delta x) = 2\Delta x a_i + z(x - \Delta x) - 2\Delta x E_t(z, \Delta x). \quad (17)$$

So the total error in calculating $z(x + \Delta x)$ is:

$$E = \frac{\Delta x^3 z'''(x_c)}{3} = O(\Delta x^3). \qquad (18)$$

The truncation error is a third order error and therefore a functional and accurate sensor can be designed using the design equations presented above with a practical number of patches. Table 1 shows the error calculation results for a simply supported beam of length ℓ. It can be seen that the error is greatly reduced with the increasing number of sensor patches. The beam lateral displacements from Eq. (19) of the simulation section is the excitation input for the sensor Eq. (7). z is also used to calculate the error in Eq. (18) while the beam lateral displacements z_m from the sensor is calculated using Eq. (14).

3. NUMERICAL SIMULATION

3.1. Numerical Simulation Equations

The forced lateral vibration steady state response of a beam can be formulated in a modal superposition form as shown in Eq. (19) :

$$z(x) \cong \sum_{k=1}^{m} W_k \psi_k(x); \qquad (19)$$

where k is the kth mode number, W_k is the modal participation factor, ψ_k is the kth mode shape, and m is the maximum number of modes used in the approximation. The output of the ith patch can be written by using Eqs. (7), (13), and (19) as:

$$\phi_i \cong -\frac{nh^f h_b h_{31}}{2\ell} \sum_{k=1}^{m} W_k \int_{x_{i-1}}^{x_i} \frac{\partial^2 \psi_k}{\partial x^2}\, dx. \qquad (20)$$

To perform the numerical simulation, we will assume that the beam is excited by a general force vector $\{f\}$ of unity magnitude applied at a node and rewrite Eq. (19) in discretized form as:[23]

$$\{z\} \cong \sum_{k=1}^{m} \frac{\{\psi_k\}\{\psi_k\}^T \{f\}}{\omega_k^2 - \omega^2 + j\eta_k\omega_k^2}; \qquad (21)$$

where ω is the excitation frequency, η_k is the structural damping factor of the kth mode, ω_k the kth natural frequency, and $j^2 = -1$. It can be shown that

$$W_k \cong \frac{\{\psi_k\}\{\psi_k\}^T}{\omega_k^2 - \omega^2 + j\eta_k\omega_k^2}. \qquad (22)$$

Equation 21 is used to calculate the response of the beam and the mode participation factor W_k to a unit input force. The output charge of each patch is then calculated using modal coordinates W_k in Eq. (20). These output charges are then used in Eq. (10) to calculate the slopes a_i at the center of each patch before calculating the bean deflection using the central-difference equation (Eq. (12)). The deflection calculated from the sensor output charge and referred to as "Measured" is compared to the deflection calculated from the mode superposition equation and referred to as "Actual." The results of the numerical simulation are discussed in the next section.

3.2. Numerical Simulation Results

The numerical simulation was performed for a simply supported, clamped-clamped, and cantilever beam. Low frequency (less than 1.5 kHz) excitation was applied to the beams using the data of Table 2. The admittance of each beam was calculated from Eq. (21), which we will refer to as an actual response, and plotted against the admittance calculated from the sensor output using Eq. (14), which we will refer to as a measured response. The admittance data was further process to extract the response of the beams at resonance for the first and second modes. These two modes were selected arbitrary for brevity. The results are shown in Figs. 3 to 8 for the three types of boundary conditions considered. Figures 3, 5, and 7 are presented to show the response of the sensor at a point over a broadband of frequency from 0-1000 Hz. For each boundary condition, the sensor accurately measures the vibration amplitude capturing all the resonance frequencies within the excitation signal. Additionally, the sensor correctly matches the response phase over the same frequency of interest. Phase is critical in sensor development because for an error sensor to be effective in applications such as active vibration or noise control, the accurate representation of the phase is crucial. The results presented in Figs. 4, 6, and 8 are showing the beam displacement curves at the first and second modes. Once again, as predicted by the admittance results, the lateral displacements of the beam predicted from the sensor match the actual displacements of the beam. It is clear that the sensors correctly "measured" the lateral deflections of the beams over a broadband

Table 2. Simulation data.

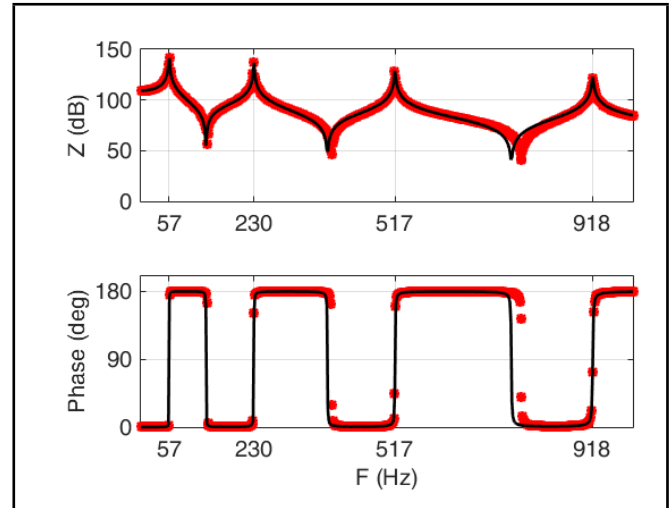| Aluminum Beam	PVDF
$\ell = 0.2$ (m)	$h^f = 50 \times 10^{-6}$ (m)
$b = 0.025$ (m)	$h_{31} = 0.4 \times 10^9$ (V/m/m/m)
$h^b = 0.001$ (m)	$\rho = 1789$ (kg/m^3)
$\rho = 2770$ (kg/m^3)	$E = 8.4 \times 10^9$ (N/m^2)
$E = 8.4 \times 10^9$ (N/m^2)	$\nu = 0.18$
$\eta = 0.002$	—

Figure 3. Beam (S-S) admittance numerical simulation (Continuous= Actual; Dot=Sensor).

frequency. However, the measurements accuracy decreases at higher frequency, which can be explained with the error inherent to the central difference approximation and the approximation of the actual deflection with mode superposition as related to the number of modes included in the computation.

4. MULTIPHYSIC SIMULATION

4.1. Multiphysic Modelling

Multiphysics or coupled physics analysis is a powerful approach that is becoming easier and more accessible due to progress in desktop computing. A multiphysic analysis is a combination of analyses from different disciplines that interact to solve a global problem. It can be used to model and analyze complex system simulations such as active noise control systems, MEMS simulation, etc. The coupling between the fields can be accomplished by either matrix coupling or load vector coupling. Load transfer can take place across surfaces or volumes depending on the application. Coupling across the fields can be complicated because different fields will be running different type of analyses during the simulation. In this work, both matrix coupling or direct methods and load vector coupling or sequential methods were used. In the sequential process, the beam structural vibration was solved first and then the results passed to the piezoeltric module. The piezoelectric analysis then proceeds using the direct method whereby the solution is obtained with a coupled element formulation. That is, the type of element used has both structural and electrical degrees of freedom.

The structural and piezoelectric coupled field analysis were used in this paper to assess the performance of the beam lateral vibration displacement curve sensor. We modeled the beam based on the data used in the numerical analysis and shown in Table 2. The theoretical mode shapes and natural frequen-
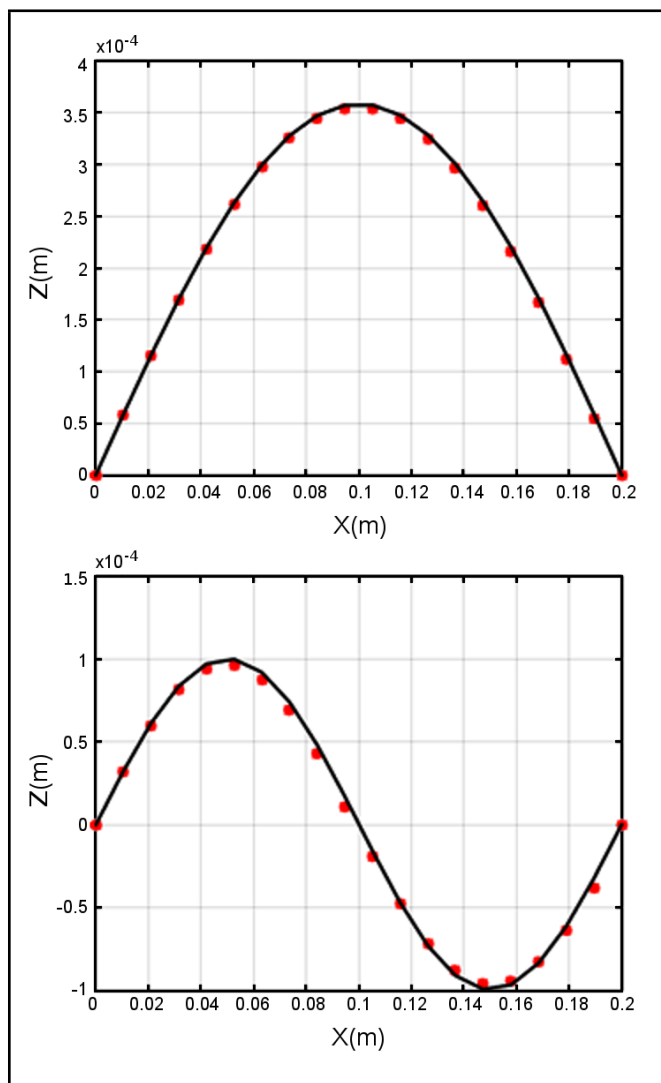
Figure 4. Beam (S-S) first and second mode response (Continuous= Actual; Dot=Sensor).
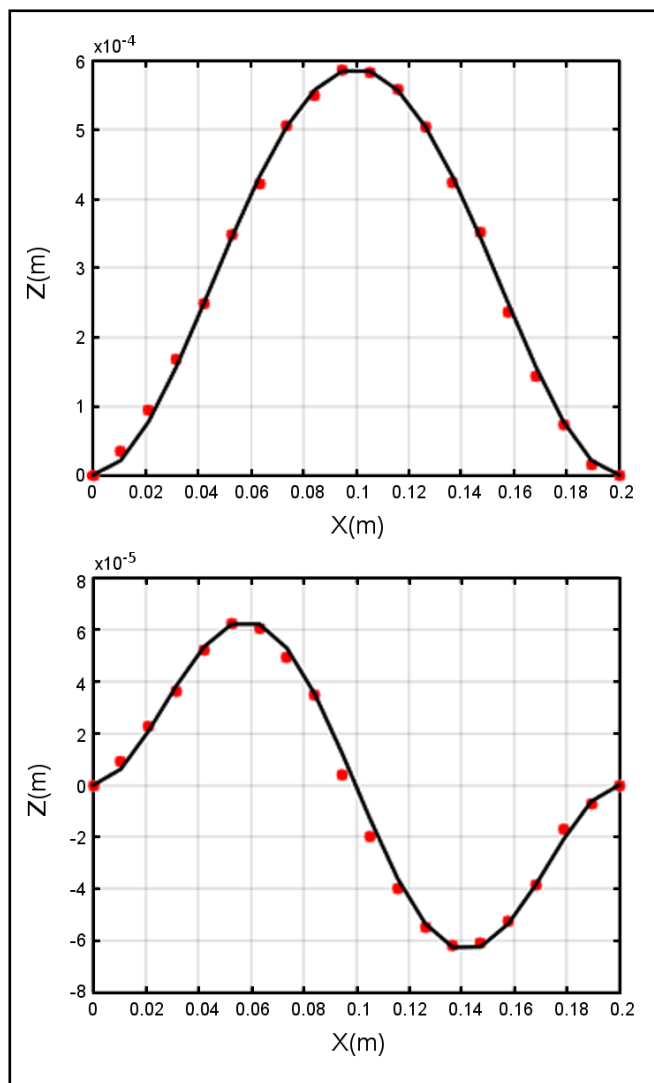

Figure 6. Beam (C-C) first and second mode response (Continuous= Actual; Dot=Sensor).
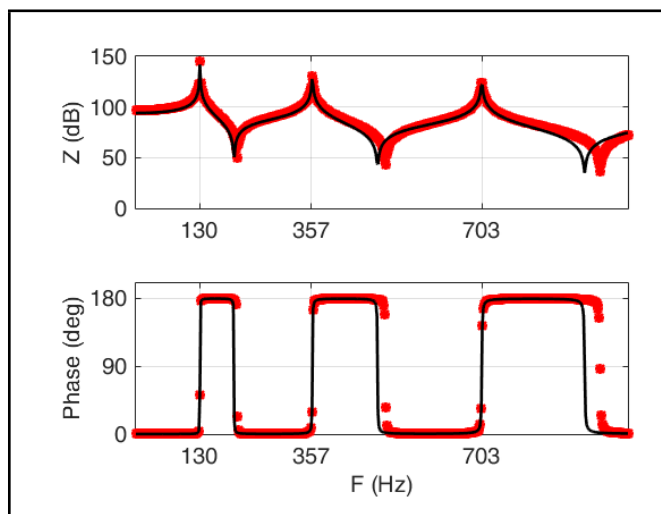

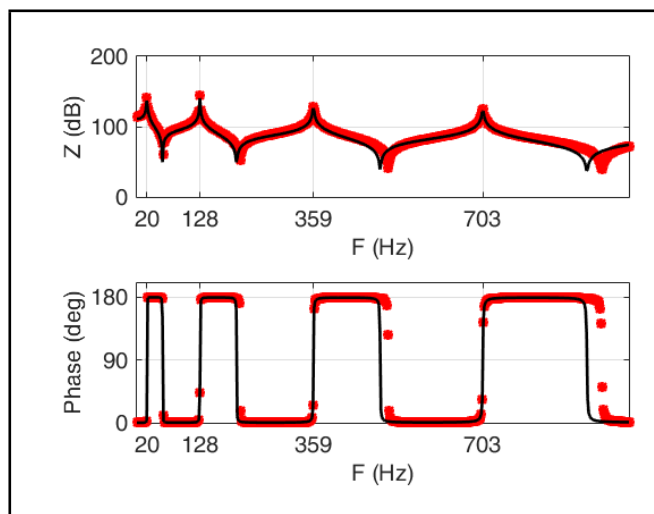**Figure 5.** Beam (C-C) admittance numerical simulation (Continuous= Actual; Dot=Sensor).

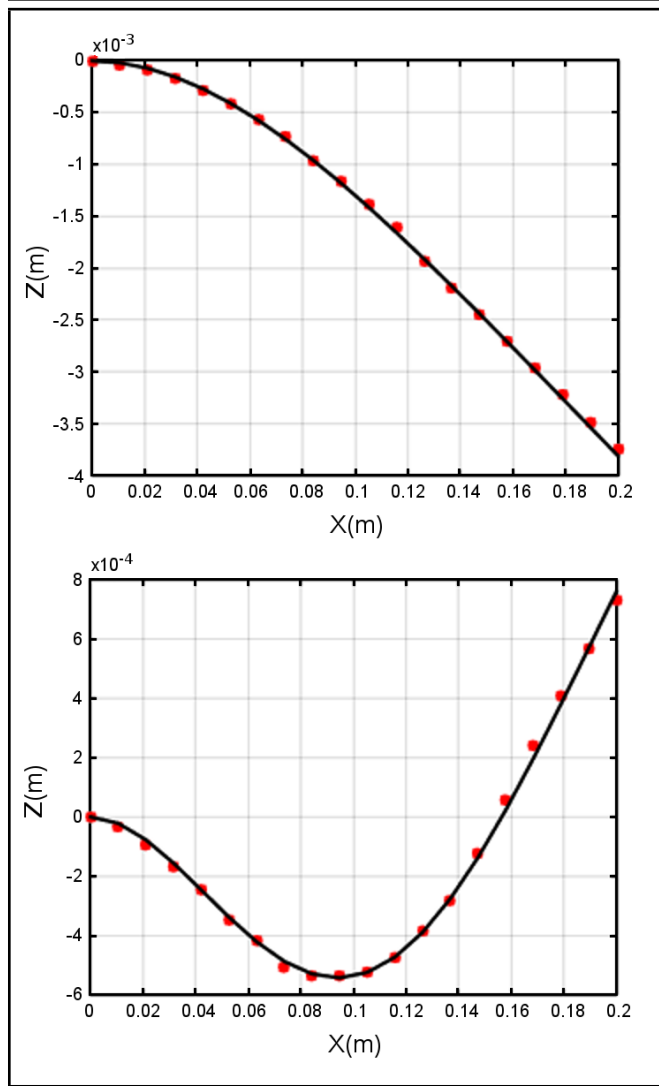**Figure 7.** Beam (C-F) admittance numerical simulation (Continuous= Actual; Dot=Sensor).

Figure 8. Beam (C-F) first and second mode response (Continuous= Actual; Dot=Sensor).

cies were matched through mesh convergence analysis with the respective structural boundary conditions for the simply supported, clamped-clamped, and cantilever beams. The film patches were then attached on top of the beam ensuring proper mesh coupling and continuity. The proper electrical and structural boundary conditions were applied to the piezoelectric elements. Because solid elements were used, simply supported boundary conditions were achieved using cylindrical supports. Figure 9 shows that cylindrical tabs were added to the ends of the beam. The tabs were constrained with fixed radial and axial displacements while the tangential displacement was free. Frequency response or harmonic analysis were carried out. The results were further processed to extract the deflection of the beams for the two first natural frequencies of each beam. These results are discussed in the next section.

4.2. Multiphysic Simulation Results

Table 3 shows the natural frequencies of the beams used in the simulation comparing the theoretical and finite element models. The theoretical values in this table are obtained using the data from Table 2 and a beam natural frequency table.[17] The finite element model analysis was carried out to assess the true performance of the sensors. Unlike in the numerical simulation, the structure was allowed to have 3D motion to ascertain
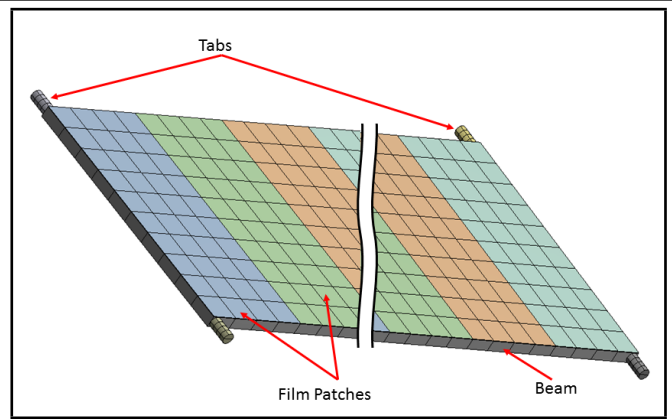

Figure 9. Beam with cylindrical tabs to simulate simply supported BC.

Table 3. The theoretical and finite element beam's natural frequencies.

Mode Number	Theoretical Natural Frequencies (Hz)			Finite Element Natural Frequencies (Hz)		
	S-S	C-C	C-F	S-S	C-C	C-F
1	57.4	130.1	20.4	57.5	130	20.5
2	229.6	358.6	128.1	229.7	358.3	128.3
3	516.5	703.1	358.8	516.0	702.2	359.2
4	918.5	1162.2	703.1	917.6	1160.3	703.7
5	1434.8	1736.1	1162.2	1425.5	1732.4	1162.8

whether or not the in plane transverse strains will greatly affect the results. In the numerical simulation, the Euler-Bernoulli beam theory was used while in the Multiphysics simulation, the output of the 3D deformation of the film was allowed. The resulting output voltages ϕ_i were used to calculate the "Measured" deflection of the beam with Eq. (14). The results shown in Figs. 10 to 15 indicate that the sensor can be used to accurately measure the deflection curve of the beams. The conclusions of the numerical simulation results can be extended to the results shown in Figs. 10 to 15. As seen in the numerical simulation, once again, the sensor is less accurate at higher frequencies. Hence, it is clear that the accuracy of the measurement is directly related to the number of patches as discussed in the error analysis section.

5. EXPERIMENTAL VERIFICATION

The sensor design theory presented and simulated above is further verified using the experimental setup shown in Fig. 16. The 482.4 mm long, 25.4 mm wide, and 3.2 mm thick aluminum beam is clamped at both ends and excited by a Labworks ET-126 shaker. The sensor is fabricated out of 28 μm thick copper-nickel metallized PVDF film. The fabrication process is displayed in Fig. 17. A template is cut out of a self-adhesive vinyl sheet by a printer-cutter as displayed in Fig. 17a. The template is laid on top of the film in Fig. 17b before an etching ink is sprayed onto the vinyl and the film. The vinyl is removed and etching chemical is applied to the film to etch away the metalized surface of the film not covered by the ink to reveal 19 segments of PVDF patches and electric connection tabs shown in Fig. 17b. Using a multi-meter, the continuity between the patches is checked to ensure that the 19 patches are electrically isolated from each other. Then, the sensor is bonded to the beam with a double sided tape and the tabs connected to the data acquisition unit with alligator clips and BNC connectors.

The beam is then excited with a unity force over broadband of frequencies from 0-800Hz. The beam Frequency Response
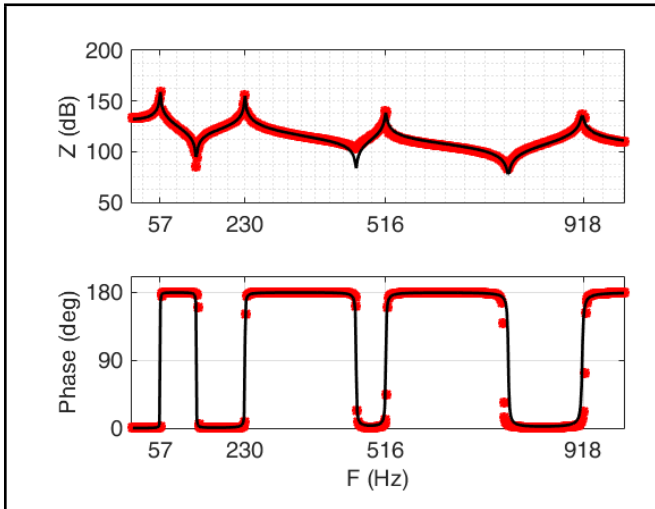
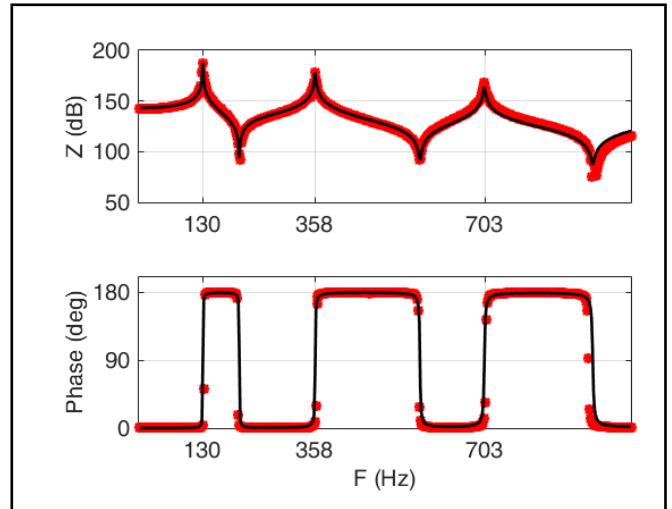**Figure 10.** Beam (S-S) admittance multiphysic simulation (Continuous= Actual; Dot=Sensor).

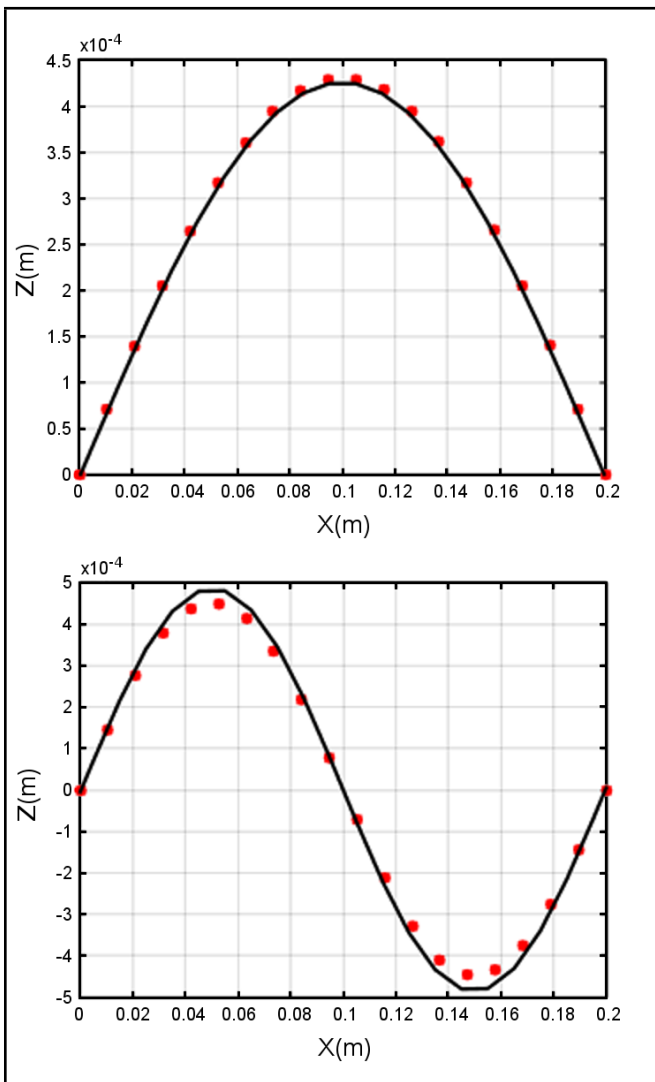**Figure 12.** Beam (C-C) admittance multiphysic simulation (Continuous= Actual; Dot=Sensor).

Figure 11. Beam (S-S) first and second mode response (Continuous= Actual; Dot=Sensor).
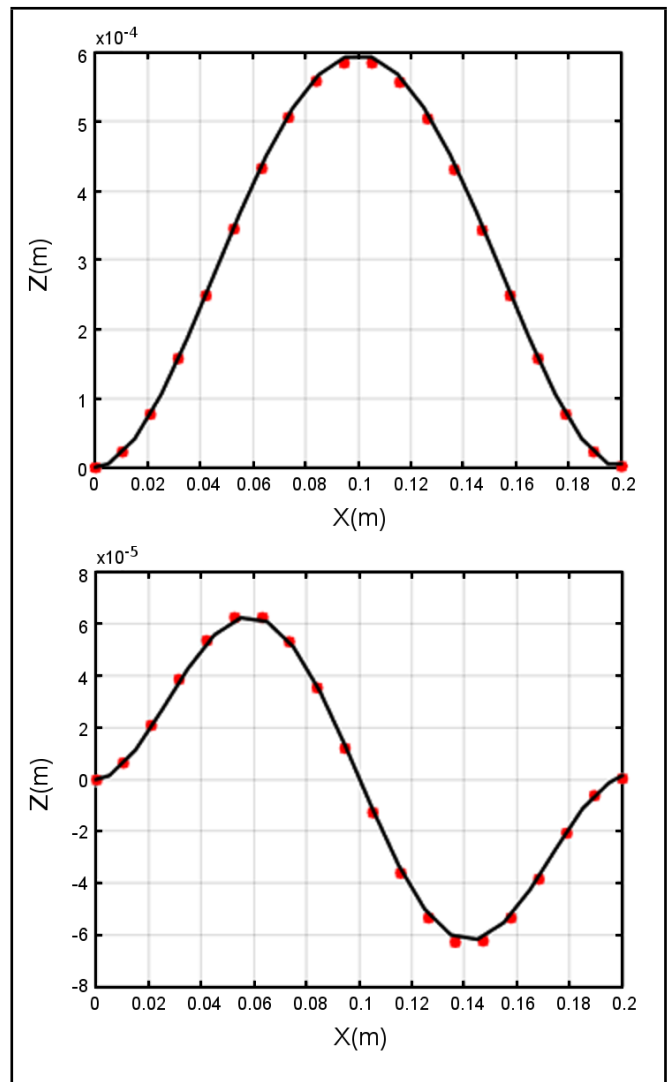

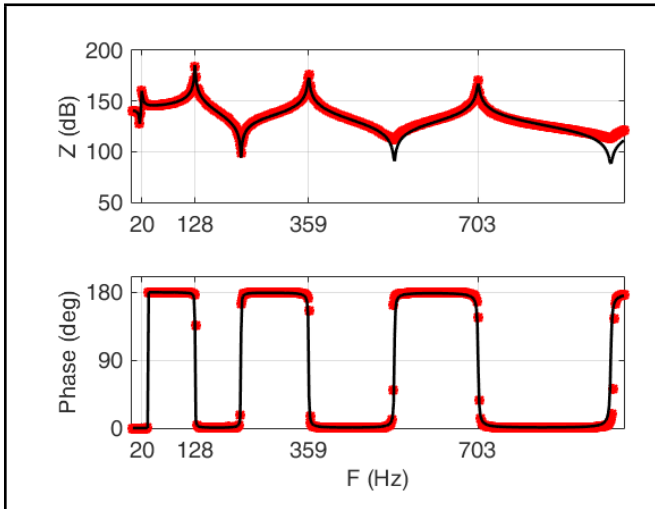**Figure 13.** Beam (C-C) first and second mode response (Continuous= Actual; Dot=Sensor).

Figure 14. Beam (C-F) admittance multiphysic simulation (Continuous= Actual; Dot=Sensor).
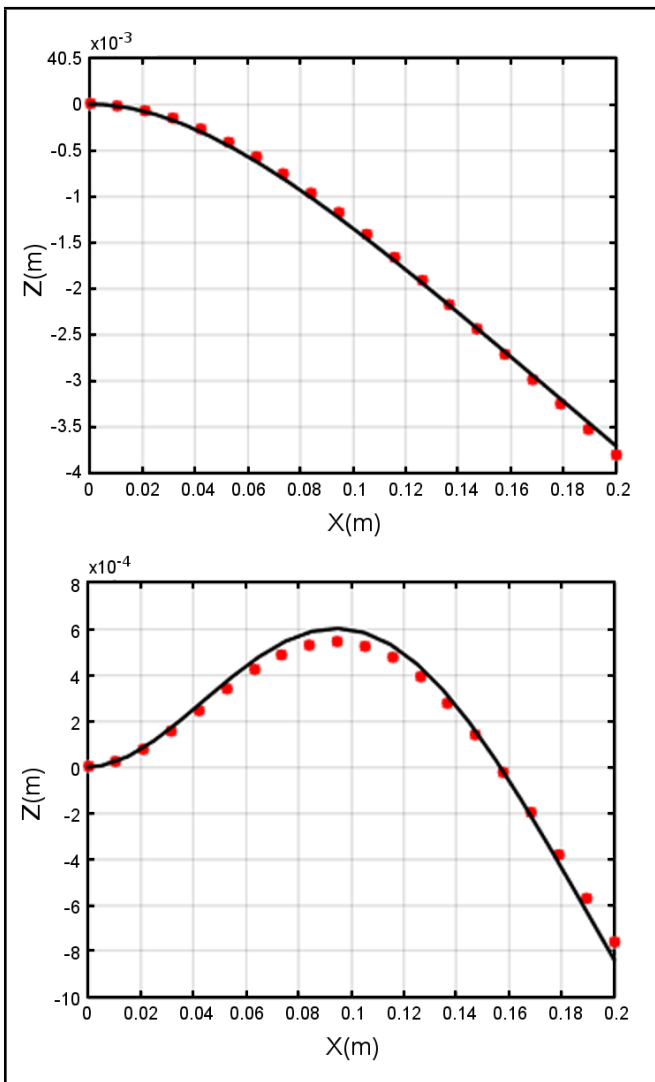

Figure 15. Beam (C-F) first and second mode response (Continuous= Actual; Dot=Sensor).

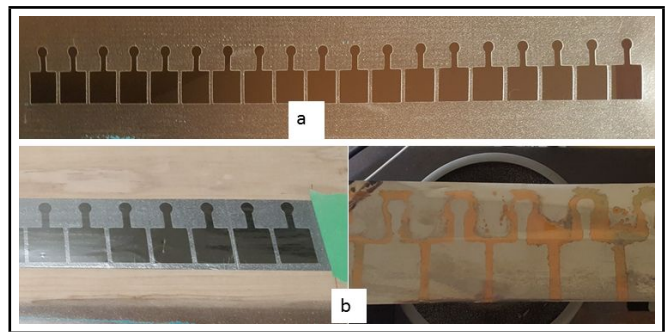**Figure 16.** Experimental setup.

Figure 17. Sensor fabrication.

Functions (FRF) are measured using a PCB 208C02 force gage as input and the sensor and a PCB 355B03 accelerometer as output. Nineteen FRFs using the sensor 19 patches are recorded and later processed using Eq. (14) to calculate the admittances of the beam from each patch. Next, a single accelerometer is used to measure the accelerance of the beam at the boundaries and at the center of the 19 segments defined by the sensor patches along the length of the beam. Then, assuming the motion to be harmonic at each frequency, the beam admittances are calculated at each measurement point by dividing the accelerance measurements by $-\omega_i^2$ where i is the ith frequency within the excitation band.

Figure 18 shows a comparison of the beam admittance at the center of an arbitrarily selected patch using the accelerometer measurements and using the PVDF sensor. The PVDF sensor measures the beam displacement accurately below 500 Hz and captures the first three modes of the beam. The sensor magnitude and phase accuracy, however, decreases beyond 500 Hz. There are three possible reasons could explain this degradation of the accuracy. The first cause could be the misplacement of the sensor on the beam. A shift along the length of the beam can result in both phase and magnitude errors. The second cause could be the limited number of sensor patches used as related to truncation errors. And the third cause could be from some imperfections in the fabrication of the sensor due to the smear of the etching chemical into the dye which will reduce the sensing surface of the patch.

The displacement curves of the beam is also calculated from the acceleration and PVDF measurements and shown in Fig. 19 for the first and second modes of the beam. It can be seen that the sensor accurately measures the vibrating beam displacement curves as expected from the plots of FRF in Fig. 18.
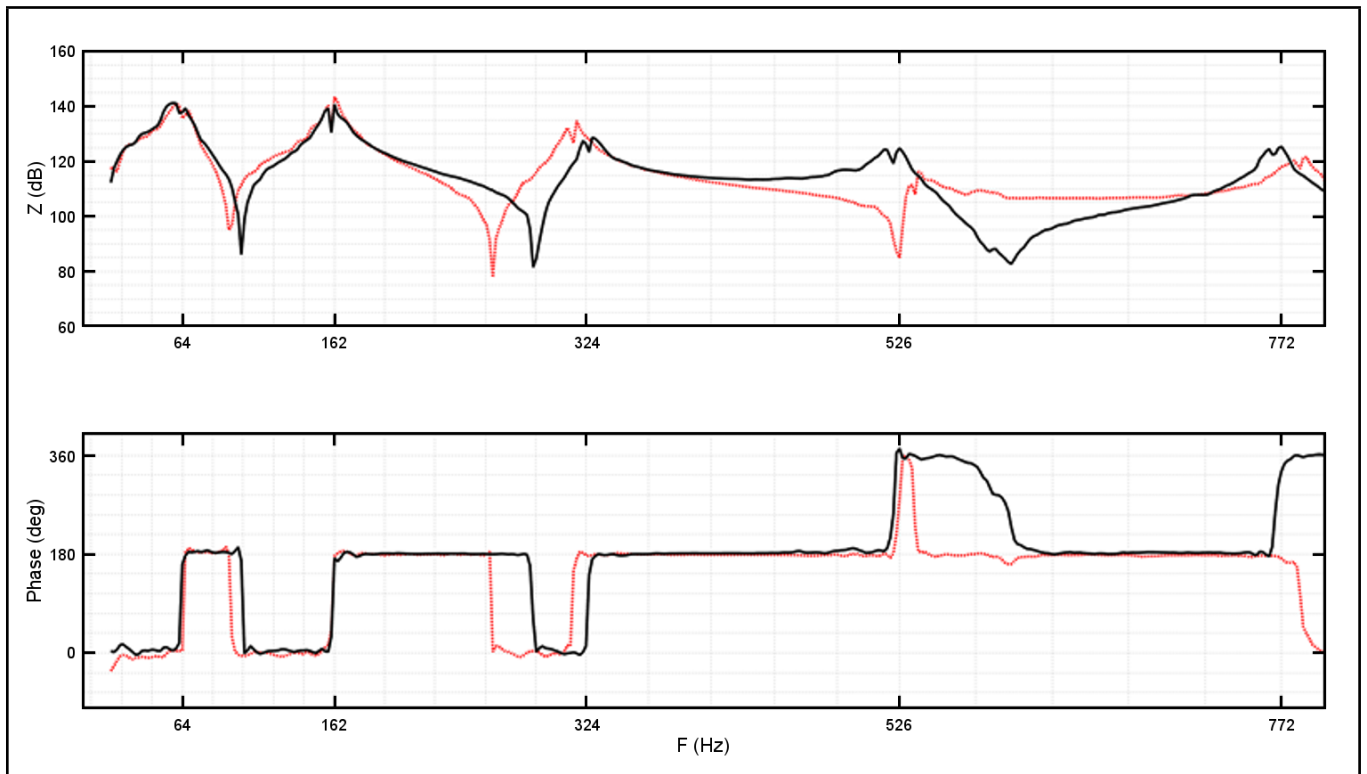
Figure 18. Admittance of experimental results (Continuous= Accelerometer; Dot=Sensor).
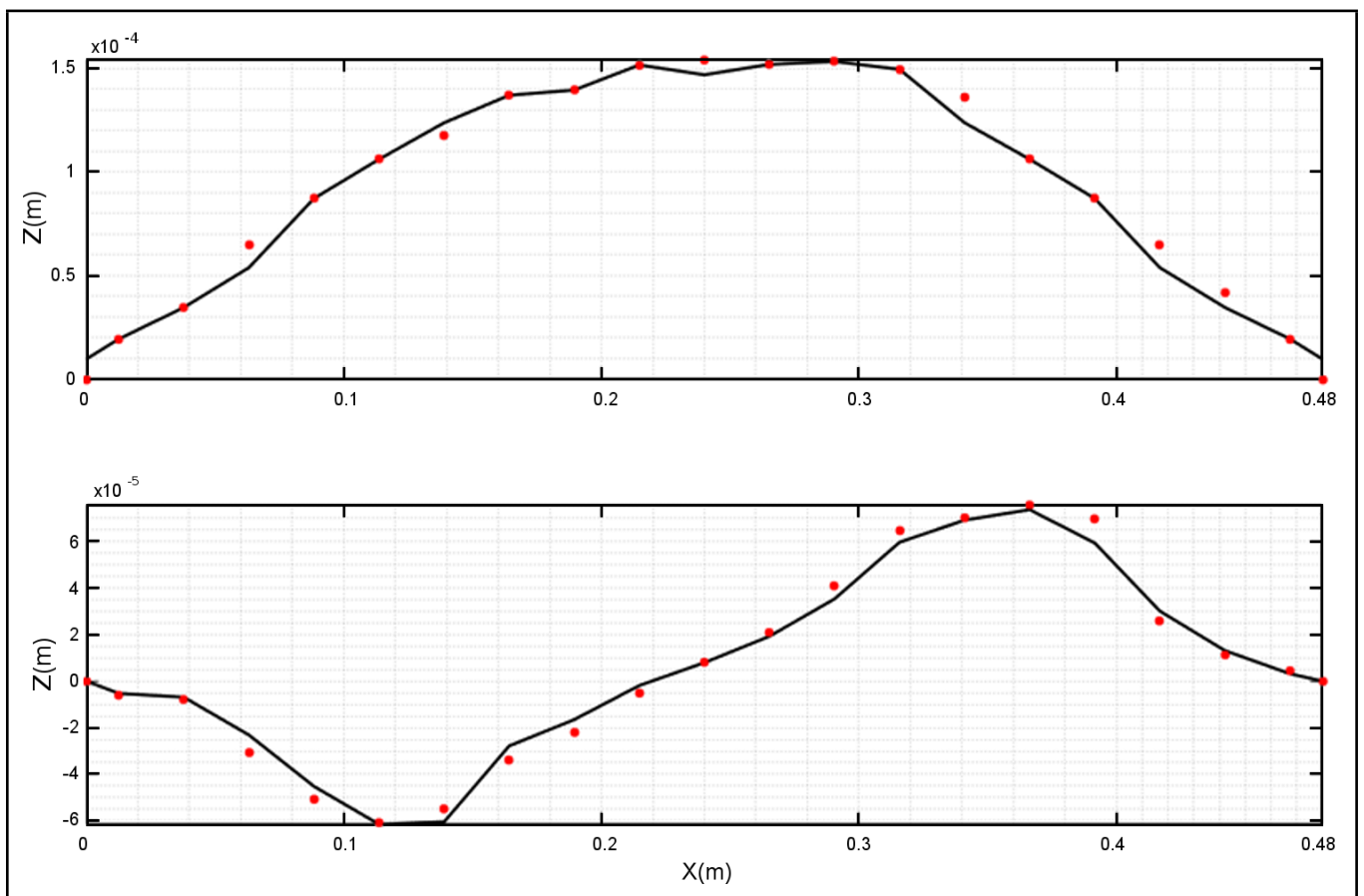

Figure 19. Beam first and second mode response (Continuous= Accelerometer; Dot=Sensor).

6. CONCLUSIONS

Equations of a beam lateral vibration displacement sensor were derived using well established one dimensional PVDF output charge equations. Bands of the piezoelectric film across the width of the beam output voltages proportional to the slops of the beam deflection curve at their respective location. These slopes were use in a central-difference equation to compute the vibration deflection curve of the beam. Truncation errors associated with the central-difference process were estimated to assert the accuracy of the sensor. The analysis resulted in a third order error term that was confirmed numerically using a simply supported beam.

The proposed sensor was verified through numerical and finite element multiphysics simulation. The numerical simulation used mode superposition and discretized models to compute the forced vibration responses of the beam over a broad band frequency. These deflection curves were compared to the deflection curves calculated using the charges from the film patches. Next a full 3D coupled physics simulation was carried out and the results used to confirm the performance of the sensor.

Furthermore, a clamped-clamped beam experimental setup was used to verify the performance of the sensor. Chemical etching process was used to fabricate the sensor and measurements were carried out using the sensor and an accelerometer. The results indicate that the 19 patches of film over 482 mm long beam accurately measured the beam lateral displacement curve up to the beam third mode.

Therefore, the work presented here proves that PVDF film can be effectively used to measure the vibration displacement curve of beams with various boundary conditions and particularly for beam with clamped-clamped boundary conditions.

REFERENCES

[1] Guigou, C. et al. Active control of sound radiation using a foam-PVDF-plate passive/active composite device, *International Journal of Acoustics and Vibration*, **2** (3), 113–118 (1997).

[2] Bailey, T. and Hubbard, J. Distributed piezoelectric polymer active vibration control of a cantilever beam, *Journal of Guidance, Control, and Dynamics*, **8** (5), 605–610, (1985).

[3] Bloomfield, P. E. Production of ferroelectric oriented PVDF films, *Journal of Plastic Film and Sheeting,* **4** (2), 123–129, (1998).

[4] Miki, H. et al. Reactive ion etching of poly (vinylidene fluoride) and its optimization, *International Journal of Engineering and Technical Research*, **3** (3), 327–333, (2015).

[5] Omidi, E.and Mahmoodi, S. N. J. Multiple mode spatial vibration reduction in flexible beams using H2- and Hinf-modified positive position feedback, *ASME Journal of Vibration and Acoustic*, **137** (1), 011016-011016-7, (2015).

[6] Adamowski, J. C., Buiochi, F., and Higuti, R. T. Ultrasonic material characterization using large-aperture PVDF receivers, *Ultrasonic*, **52** (2), 110–115, (2010).

[7] Kryger, M., Eiken, T., and Qin, L. The use of combined thermal/pressure polyvinylidene fluoride film airflow sensor in polysomnography, *Springer-Verlag Berlin Heidelberg*, 1267–1273, (2013). http://dx.doi.org/10.1007/s11325-013-0832-5

[8] Banerjee, T. et al. Active control of radiated sound from stiffened plates using IDE-PFC actuators, *International Journal of Acoustics and Vibration*, **18** (3), 109–116, (2013).

[9] Tamjidi, et al. PVDF actuator for high-frequency fatigue test of thin-film metals, *IEEJ Transaction on Electronic and Electronic Engineering*, **8** (2), 199–205, (2013).

[10] Tung, C. Y. Precision microscopic actuations of parabolic cylindrical shell reflectors, *ASME Journal of Vibration and Acoustic*, **137** (1), (2015).

[11] Lee, C. K. and Moon, F. C. Modal sensors/actuators, *Trans. ASME*, **57**, 434–441, (1990).

[12] Clark, R. L., Flemming, M. R., and Fuller, C. R. Piezoelectric actuators for distributed vibration excitation of thin plates: A comparison between theory and experiment, *ASME Journal of Vibration and Acoustic*, **115** (3), 332–339, (1993).

[13] Zahui, M., Kamman, J., and Naghshineh, K. Theoretical development and experimental validation of local volume displacement sensors for a vibrating beam, *ASME Journal of Vibration and Acoustics*, **123** (1), 110–118, (2001).

[14] Ribeiro, P., Alves, L., and Marinho, J. Experimental investigation on the occurrence of internal resonances in a clamped-clamped beam, *International Journal of Acoustics and Vibration*, **6** (3), 169–173, (2001).

[15] Ding, J. et al. Fatigue life assessment of traffic-signal support structures from an analytical approach and long-term vibration monitoring data, *Journal of Structural Engineering*, **142** (6), 1–12, (2016).

[16] McManus, P. S. et al. Damping in cantilevered traffic signal structures under forced vibration, *Journal of Structural Engineering*, **129** (3), 373–382, (2003).

[17] Rao, S. , *Mechanical vibrations*, Addison-Wesley 4th edition, (2004).

[18] Salo, J.and Korhonen, I. Calculated estimate of FBG sensor's suitability for beam vibration and strain measuring, *Measurement*, **47**, 178–173, (2014).

[19] Tzou, H. S. *Piezoelectric Shells*, Kluwer Academic Publishers, Dordrecht, Boston, London, (1993).

[20] Feng, K.and Shi, Z. *Mathematical Theory of Elastic Structures*, Springer New York, ISBN 0-387-51326-4, 1981.

[21] Zahui, M., and Thomas, R. Design of beam surface displacement sensors, *ASME International Mechanical Engineering Conference and Exposition*, 1–7, 2014.

[22] Kreyszig, E. *Advanced Engineering Mathematics*, 10th Edition, ISBN-13: 978-0470458365, 2011.

[23] Ewins, D. J. *Modal Testing: Theory, Practice and Application*, 2nd Edition, research Studies Press Ltd, Baldock, Hertfordshire, England, 1984.